RSC Advances

PAPER

View Article Online
View Journal | View Issue

Cite this: *RSC Adv.*, 2025, **15**, 2890

Electron paramagnetic resonance and photoluminescence study on local structure of Gd^{3+} ions in Gd-doped CaF_2 crystals†

Shirui Luo,[abc] Fang Tan,[b] Dapeng Jiang,[a] Honggang Liu,[f] Tingyu Liu,[g] Liening Wei,[b] Yu Liu,[ac] Zhen Zhang,[a] Fengkai Ma,[e] Zhonghan Zhang,[a] Huamin Kou,[ac] Huaize Qin,[bd] Jingguo Zhu,[b] Junjie Hu,[b] Wei Hong *[b] and Liangbi Su *[ac]

Received 7th December 2024
Accepted 22nd January 2025

DOI: 10.1039/d4ra08622h

rsc.li/rsc-advances

Employing electron paramagnetic resonance (EPR) and excitation and photoluminescence (PL) spectra, changes of the local structure of Gd^{3+} ions were investigated for the CaF_2 crystals containing 0.00015, 0.17, 1.22, 5.75 at% Gd ions, respectively. The obtained spin Hamiltonian parameters of the cubic configuration Gd^{3+} monomer are $g = 1.9862$, $B_4 = -2.3153 \pm 0.015$ MHz and $B_6 = -0.0005 \pm 0.001$ MHz. The peak-to-peak width of the EPR lines of the cubic configuration Gd^{3+} is significantly broadened and partially quenched with the increase of the Gd^{3+} concentration, which indicates that the exchange and dipole interactions between Gd^{3+}–Gd^{3+} are enhanced. From theoretical calculations, combined with experimentally measured angular dependence, we found that for the 1.22 at% Gd:CaF_2 crystals, Gd^{3+} remains essentially cubic, and the majority of the Gd^{3+} ions are distributed as a dimer conformation along the [110] direction and at a distance of about 7.7 Å.

1. Introduction

Due to the high intensity and short pulse duration, ultra-intense ultrashort lasers show great promise for applications in basic and cutting-edge interdisciplinary disciplines, such as high-energy physics, fusion energy, precision measurements, chemistry, materials, and biomedicine.[1–4] The invention of the chirped pulse amplification (CPA) technique has greatly increased the peak power of pulsed lasers.[5] As the basis for realizing the CPA technique, the development of laser materials that satisfy all relevant specifications has been of great interest. So far, due to the excellent comprehensive material parameters, two laser gain media, Nd-glass and Ti:sapphire, have been widely used in ultra-intense and ultra-short lasers. However, with the development of ultra-intense ultrashort lasers toward higher peak power, as well as higher repetition frequency and average output power, both materials show obvious limitations. The lower thermal conductivity of the Nd-glass medium limits its application to high repetition frequency lasers,[6] and the stronger amplification of spontaneous emission (ASE) of Ti:sapphire limits its maximum output energy to tens of joules.[7]

Nd^{3+} ion-doped alkaline-earth metal fluoride (MF_2) crystals have excellent properties of high thermal conductivity (10 W m^{-1} K^{-1}) and wide photoluminescence bands (20–30 nm), which makes them an important potential gain medium for high-repeating-frequency, high-power ultrashort lasers.[8–11] Kaminskii *et al.* have extensively studied Nd^{3+} doped MF_2 crystals since the 1960s. In order to solve the severe concentration quenching that occurs in the luminescence of Nd^{3+} ions in the 1 μm band when they are highly doped with Nd^{3+} ions, one needs to introduce Y^{3+}, La^{3+}, Gd^{3+} or Lu^{3+} at a concentration of about 5 at% as buffer ions into Nd^{3+} doped fluoride crystals in order to ensure the quantum efficiency of their photoluminescence.[12–15] In recent years, Qin *et al.* achieved the shortest mode-locked pulse of 103 fs by choosing a suitable Y doping concentration (10%).[16] Tang *et al.* synthesized 0.5% Nd, 5% Y:CaF_2 crystal rods as an amplifying medium with high repetition frequency and achieved a small gain of 2.7, which is close to twice that of Nd-glass.[17]

Buffer ions doped with Nd:MF_2 will come close to Nd^{3+} ions, decrease the symmetry of the local environment of Nd^{3+} ions and increase the distance between Nd^{3+} ions, thus eliminating the

[a]State Key Laboratory of High Performance Ceramics and Superfine Microstructure, Shanghai Institute of Ceramics, Chinese Academy of Sciences, Shanghai 201899, China
[b]Laser Fusion Research Center, Mianyang, Sichuan, 621900, China
[c]Center of Materials Science and Optoelectronics Engineering, University of Chinese Academy of Sciences, Beijing 100049, China
[d]State Key Laboratory of Crystal Materials, Shandong University, Jinan 250100, China
[e]Department of Optoelectronic Engineering, Jinan University, Guangzhou 510632, China
[f]College of Materials Science and Engineering, Sichuan University, Chengdu 610064, China
[g]College of Science, University of Shanghai for Science and Technology, Shanghai, 200093, China

† Electronic supplementary information (ESI) available. See DOI: https://doi.org/10.1039/d4ra08622h

concentration quenching of Nd^{3+},[18] and thus higher doping concentration is required. Phenomenologically, large doping brings about defects such as small-angle grain boundaries (SAGB), which leads to an order of magnitude decrease in optical uniformity[19] and reduces the laser-induced damage threshold,[20] which affects the stable application of MF_2 in highly heavy-frequency and ultrafast high-power lasers. The specific physical processes responsible for these unfavorable effects of high-concentration doping are not fully understood, and it is necessary to study the local structure of high-concentration doped trivalent rare-earth ions in MF_2 crystals, which will help to find a way to improve the quality of the crystals.

The local structures formed by the doping of high concentrations of trivalent rare earth ions in alkaline earth metal fluorides are very complex and have been studied for sixty years. At low doping concentrations of a few ppm, the local structures are dominated by spatially discrete monomers, such that the monomers often exhibit different local symmetries due to the different ways of charge balance. At doping concentrations reaching greater than 100 ppm,[21] dimers, trimers, and even hexamers appear. Experimentally, some of these clusters have been successfully obtained by different methods. Using fluorescence spectroscopy[22] and selective excitation,[23] fluorescence signals from a variety of photoactive centers have been observed in crystals. Subsequently, Andeen *et al.* observed cluster-associated dielectric relaxation.[24] Catlow *et al.* observed the way in which the local structural environment of the impurities varies with the size of the rare-earth ions by extended X-ray absorption fine structure (EXAFS), and obtained under- and over-doped dimeric and hexametric configurations by computer lattice simulation studies.[21] The study of F-occupancy using neutron diffraction revealed that the dominant multimer in 5% La-doped CaF_2 is a spatially discrete distribution of dimer,[25] as well as a model of polymers in higher concentration Y-doped CaF_2 sample.[26] On the other hand, some progress has been made in related computer simulations. Ma *et al.* obtained a series of cluster configurations of rare earth ions doped in CaF_2 and SrF_2 matrices using first-principles calculations based on density-functional theory.[27–29]

Electron paramagnetic resonance (EPR), as a characterization tool for the study of unpaired electrons, has been widely used in the past decades to determine the monomer structure of low concentration doped trivalent rare earth ions in MF_2,[30–36] and EPR studies on the cluster structure of high concentration doped trivalent rare earth ions are also being carried out. Aminov *et al.* investigated cerium doped CaF_2 single crystals, and observed a broadening of EPR spectra at high concentrations (5–15 at%).[37] Kazanskii *et al.* measured the tetragonal antiprismatic prismatic structure of trivalent lanthanide ions (Ln^{3+}) in single crystals of Ln^{3+} doped MF_2 above 1 at% using EPR, and the symmetric hexametric model was established by computer simulation.[38] Among the trivalent rare-earth ions, Gd^{3+} has seven electrons in 4f orbital and the ground state is $^8S_{7/2}$ because its orbital angular momentum is zero, and for its dimer EPR Hamiltonian quantities contain fewer interaction terms inside the description. In addition, the spin-lattice relaxation time of Gd^{3+} is quite long, and its EPR signals can be easily obtained even at room temperature, which makes it a very good sample that can be used to study the local structure of the clusters by EPR.

In order to further investigate the localized structure of doped Gd^{3+} ions in MF_2 crystals, we grew Gd^{3+}:CaF_2 crystals with nominal concentrations of Gd of 0.17, 1.22 and 5.75 at% named 0.1GCF, 1GCF and 5GCF, and 0.005 at% Nd^{3+}:CaF_2 crystals containing trace Gd impurities at a concentration of only 1.5 ppm named NCF. These four samples containing different concentrations of Gd ions were characterized using EPR, excitation and PL spectroscopy, XRD, and ICP-MS. EPR experiments revealed that the main EPR spectrum of the NCF sample at room temperature belongs to the Gd^{3+} paramagnetic center in cubic field. By fitting the experimental data to the angular dependence of the EPR spectrum of this paramagnetic center, we obtained the spin Hamiltonian parameters of the Gd^{3+} monomer in the cubic configuration. Further, we obtained the EPR spectra of all samples when the magnetic field was parallel to the *c*-axis of the crystals. The results show that all these crystals contain EPR lines corresponding to the Gd^{3+} centers in the cubic field, and the peak-to-peak EPR line width grows from 7 G to 158 G nearly linearly as the concentration of Gd increases. This increase in width is related to the exchange interaction (EI) and magnetic dipole–dipole interaction (MDDI) of Gd^{3+} ions in the dimer, and this result is consistent with the expectation that dimers, or even high-order clusters, are formed from the cubic conformation Gd^{3+} centers in the samples as the concentration of Gd increases.

2. Experiments

The 0.1GCF, 1GCF and 5GCF samples used in this study were grown from 4N CaF_2 blocks and 4N GdF_3 powder by Bridgeman method. The NCF samples were grown from 4N CaF_2 blocks and 4N NdF_3 powder by the same method. Crucibles made of high-purity platinum were used as carriers for the crystal feedstock, and 1 wt% polytetrafluoroethylene (PTFE) micropowder was added as a deoxidizing agent. The target temperature controlled by the program is 1430 °C, the heating rate is 40–100 °C h^{-1}, and after holding for 3–5 hours, the guide tube is slowly lowered at a rate of 0.8 mm h^{-1} to enter the crystal growth stage. Crystal growth time is set at 230 hours. After the crystal growth is complete, the crystal begins to cool down at a rate of 60 °C h^{-1}. The three samples were obtained from the same batch in a single growth run, and underwent the same descending process, resulting in columnar samples with a diameter of about 2.5 cm and a length of about 9 cm. The elemental content of Gd in the samples was determined using inductively coupled plasma mass spectrometry (ICP-MS), and the results are shown in Table 1. The sample powders were subjected to XRD tests at room temperature using a high-resolution X-ray powder diffractometer, which was used to obtain information on the structure and lattice constants of the crystals. The crystals were cut after high-precision orientation with a non-standard high-speed fully automated Laue single-crystal orienter to obtain the experimental samples for EPR tests, which were rectangular in size of 3 × 3 × 5 mm^3. The three edges of the samples were parallel to the axes *a*, *b*, and *c* of the crystals respectively, which were equivalent.

Table 1 The studied Gd concentration of CaF_2 single crystals

	NCF	0.1GCF	1GCF	5GCF
Gd (at%)	0.00015	0.17	1.22	5.75

The nomenclature of *a*, *b*, and *c* was arbitrary. The EPR measurements were carried out using a continuous-wave EPR spectrometer of X-band. The microwave frequency was close to 9.86 GHz. Modulation amplitude of the NCF is 1 G, and which of the 1GCF is 8 G. The modulation frequency was 100 kHz. The magnetic field measurement error was less than 1 G after calibration of the magnetic field with a standard strong pitch sample. PL spectra were recorded with an Optical Parametric Oscillator (OPO) laser excitation and a time-resolved fluorometer. The cryogenic PL spectra were measured by immobilizing the samples in a helium cryostat at a temperature of 16 K.

First-principles calculations were used to further validate this structure. The 2 × 2 × 2 supercells were constructed to simulate CaF_2 crystals with point defects one Gd_{Ca} or two Gd_{Ca}, as shown in Fig. 4. We optimized the supercell structure using density functional theory (DFT) and the Vienna *Ab initio* Simulation Package (VASP). The projector augmented wave (PAW) method was employed for the potential field, with a cutoff energy of 680 eV. The Monkhorst–Pack *k*-point meshes of 5 × 5 × 5 were used. The Perdew–Burke–Ernzerhof (PBE) functional, based on the generalized gradient approximation (GGA), was utilized for the electron exchange and correlation functions. To accurately model the excited states in the system, the Hubbard *U* parameter was employed. The value of the d-orbital of the Gd atom is 6 eV.[39] The convergence criteria for force and energy were met with thresholds set at 0.001 eV $Å^{-1}$ and 10^{-6} eV, respectively. Atomic configurations of Ca $3s^2p^64s^2$, F $1s^22s^2p^5$ and Gd $5s^2p^6d^16s^2$ were treated as valence electrons.

3. Results

3.1 EPR results

The EPR spectrum of the NCF and 1GCF samples with magnetic field parallel to the *c*-axis of the crystal at room temperature is shown in Fig. 1(a) and (b). When the microwave frequency is 9.86 G, similar 7 distinct EPR lines are observed in the EPR

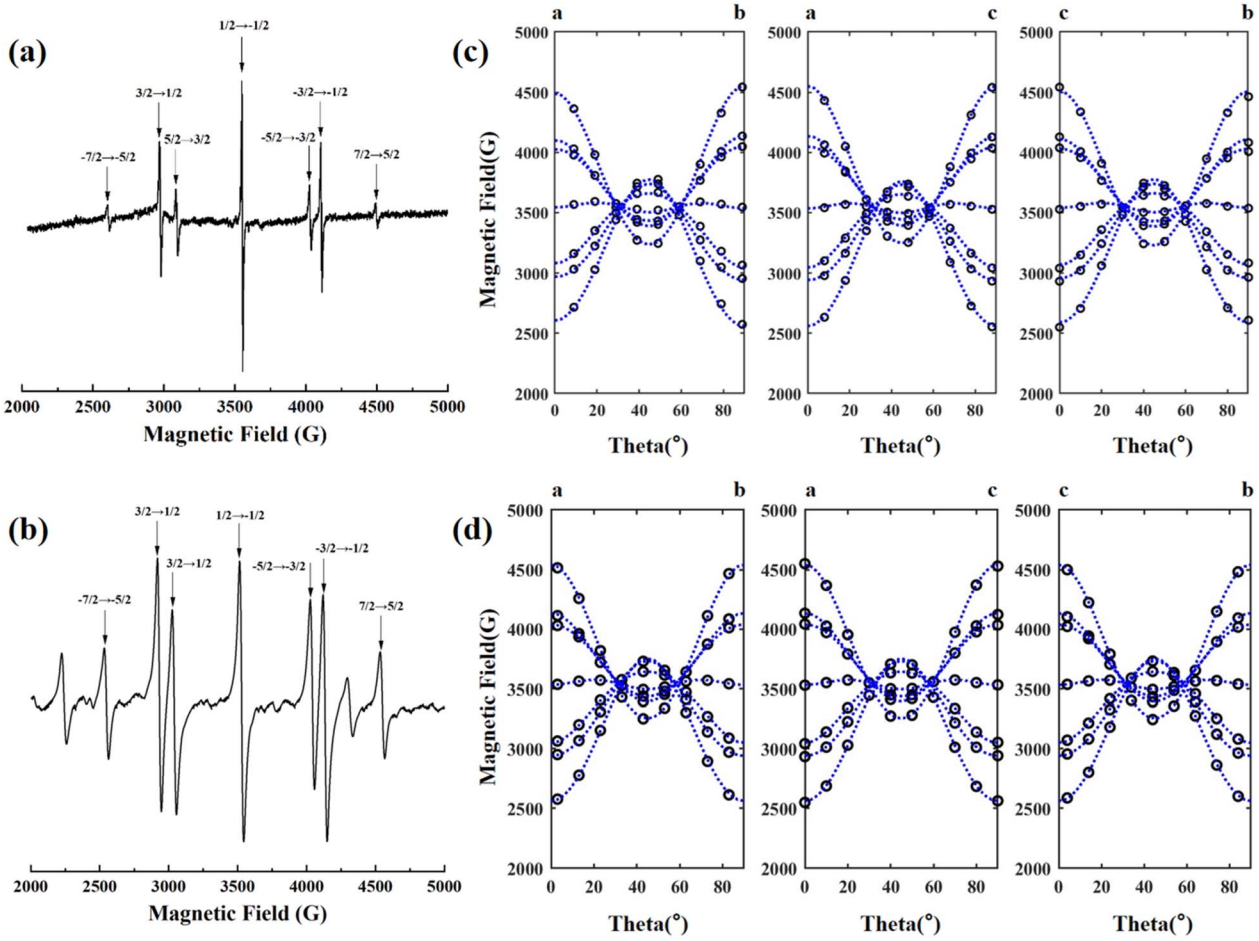

Fig. 1 Electron paramagnetic resonance spectra of (a) NCF and (b) 1GCF crystals at room temperature with ν = 9.86 GHz, B//c. Modulation amplitude of the NCF is 1 G, and which of the 1GCF is 8 G. Angular dependence of the EPR spectra of the Gd^{3+} center at room temperature in the (c) NCF and (d) 1GCF crystals with the magnetic field lying in the *a*–*b*, *a*–*c* and *c*–*b* plane. Each hollow circle represents a measured EPR line and the blue dashed lines are the angular dependence of the resonance fields calculated using the fitted spin Hamiltonian parameters in Table 2.

spectra of NCF and 1GCF. Although NCF sample contains higher concentration of Nd^{3+} ions, the EPR resonance lines for Nd^{3+} ions do not appear at room temperature.

In order to obtain the complete spin Hamiltonian parameters, the angular dependence of these seven EPR lines in the planes of the crystals *a*–*b*, *a*–*c* and *c*–*b* were measured by using a homemade correlator, and the results are shown in Fig. 1(c) and (d). Experimental data were collected at 10° intervals and each hollow circle represents a measured resonance line.

The angular dependence of the EPR lines in the three planes shows the same pattern. When the direction of the scanning magnetic field relative to the crystal axis is changed, the EPR lines split and merge with the rotation of the magnetic field. When the magnetic field is parallel to the *a*, *b* and *c* axes of the crystal, the splitting between the seven EPR lines is the largest, and the obtained EPR spectrum is shown in Fig. 1(a). The fine structure is seen to collapse from the [100] direction when the magnetic field is at an angle of about 30° and 60° to the *c*-axis.

The high concentration of doped Gd^{3+} ions have a significant effect on their EPR spectra at room temperature. We measured the EPR spectra of four crystals, NCF, 0.1GCF, 1GCF and 5GCF, when the magnetic field is parallel to the *c*-axis, and the results are shown in Fig. 2(b). In very close proximity to the seven EPR spectral lines of the NCF crystal, the three highly doped samples have similar seven resonance lines. Taking the EPR line of 4497 G in Fig. 1(a) as an example, the positions of the EPR lines for the three crystals of 0.1GCF, 1GCF, and 5GCF are shifted by 45 G, 30 G, and 40 G. The EPR spectra of the three crystals of NCF, 1GCF and 5GCF are dominated by these seven EPR lines, but the 0.1GCF crystal contains a large number of other resonance lines of comparable intensity. The intensities of the seven EPR lines increase proportionally with increasing doping concentration below 1 at%, but when the concentration increases to 5 at%, the integral area decreases instead. The peak-to-peak widths of the EPR lines located near 3552 G are 7 G, 12 G, 29 G and 158 G, respectively, as the doping concentration increases.

3.2 Excitation and PL spectra results

The excitation and PL spectra of the samples are shown in Fig. 2(c) and (d), and the NCF sample could not be detected due to the Gd content of only 1.5 ppm. The excitation spectrum is shown in Fig. 2(c), and the monitored emission peak wavelength is 314 nm, and it can be seen that the excitation peaks were detected at 245.4 nm, 247.2 nm, 253.2 nm, 273.0 nm, 275.6 nm and 278.6 nm. The PL spectra are shown in Fig. 2(d),

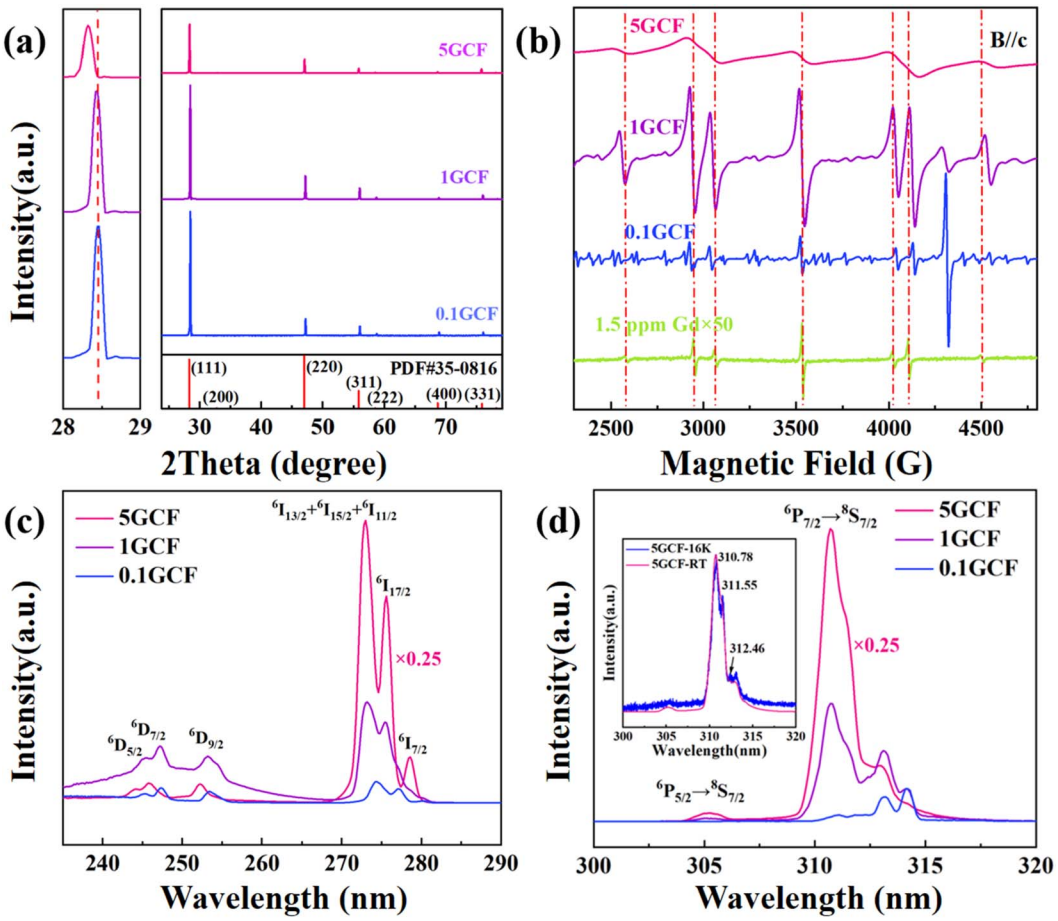

Fig. 2 (a) High-resolution X-ray diffraction (XRD) patterns of 0.1GCF, 1GCF and 5GCF; (b) EPR spectra of NCF, 0.1GCF, 1GCF and 5GCF crystals at room temperature with $\nu = 9.86$ GHz. B//c. Modulation amplitude is 8 G; (c) excitation and (d) PL spectra of 0.1GCF, 1GCF and 5GCF crystals at room temperature, the intensity of 5GCF was multiplied by 0.25 for clear view.

and there are two sets of emission peaks at around 305 nm and 314 nm. The intensity of the excitation and PL peaks gradually increases with increasing doping concentration. The low-temperature (16 K) PL spectrum of 5GCF was tested, and the normalized PL spectrum is shown in Fig. 2(d), three emission peaks at 310.78 nm, 311.55 nm and 312.46 nm were observed.

4. Data analysis and discussion

4.1 The Hamiltonian parameters of the Gd^{3+} monomer

Before investigating the cluster structure of Gd^{3+}, it is first necessary to fit the Hamiltonian parameters of the Gd^{3+} monomer by studying low concentration samples, and accurate monomer spin Hamiltonian parameters are the necessary basis for describing the dimer EPR angular dependence. Seven characteristic EPR resonance lines were observed in both 1.5 ppm Gd samples and samples doped with different concentrations of Gd, with positions and angular dependence consistent with the cubic field Gd^{3+} reported.[40,41] The model of nonlocally compensated cubic Gd^{3+} centers in the crystal structure of MF_2 is formed by the substitution of Gd^{3+} ions for the divalent cation Ca^{2+}. With Gd^{3+} at the center of a simple cube consisting of eight fluoride ions, the required charge compensator is located far enough away from the Gd^{3+} ions so that the cubic symmetry at Gd^{3+} is ensured.[42] Thus, the observed EPR spectrum of the cubic field of the Gd^{3+} ion in CaF_2 and its dependence on the angle is described by a spin Hamiltonian $\hat{H}$ as follows:

$$\hat{H} = \beta_e \boldsymbol{B}^T \overleftrightarrow{g} \hat{\boldsymbol{S}} + B_4\left(\hat{O}_4^0 + 5\hat{O}_4{}^4\right) + B_6\left(\hat{O}_6^0 - 21\hat{O}_4{}^4\right) \quad (1)$$

where β_e is the Bohr magneton, g is the Landé factor, $\boldsymbol{B}$ is the applied magnetic field, $\hat{\boldsymbol{S}}$ is the effective spin operator, $\hat{O}_m{}^n$ is the Stevens operators.[43] B_m is the corresponding coefficiency, *i.e.*, fourth-order and sixth-order zero-field splitting parameters.

In eqn (1), the first term is the electron Zeeman term, and the second and third terms represent fine-structure splitting of the $^8S_{7/2}$ ground state due to the crystal-field. The symmetric g-matrix requires six independent parameters, including three principal values and three Euler angles to specify the molecular coordinates relative to the crystal coordinates. In this work, the three principal values of the g tensor are set equal, and B_4 and B_6 are two independent higher-order crystal field constants. We performed a least-squares fit to the angular dependence of Fig. 1(c) and (d) using eqn (1) with the three independent parameters of g, B_4 and B_6. The fitting process precisely diagonalizes the Hamiltonian matrix of eqn (1). The fitting results are shown in Table 2. It can be seen that the parameters of our fitted cubic configuration do not differ much from the literature.[40,41] The calculated curves of the angular dependences were obtained using the fitting values from Table 2, as shown by the blue dashed line in Fig. 1(c) and (d). It can be seen that the value of the Landé factor $g_{NCF} = 1.9862$ and $g_{1GCF} = 1.9889$. If the ground state of the $4f^7$ ions were a pure $^8S_{7/2}$ state, the only non-zero interaction in a magnetic resonance experiment would be the Zeeman interaction, and g would be isotropic and very close to the free spin value of 2.00232. Shifts of the principal values from the free-spin value are caused by spin–orbit interactions.[44] In subsequent work, *ab initio* calculations of the g-factor values can be carried out using the multi-configuration response theory.[45]

Table 2 Spin Hamiltonian parameters and deviation for cubic Gd^{3+} centers in CaF_2 single crystals obtained by angular dependence fitting

Ref. 40	g	1.991 ± 0.002
	B_4	−2.3109 ± 0.025 MHz
	B_6	−0.0024 ± 0.0012 MHz
Ref. 41	g	1.9918 ± 0.0010
	B_4	−2.3284 ± 0.015 MHz
	B_6	−0.0035 ± 0.0015 MHz
NCF	g	1.9862 ± 0.0007
	B_4	−2.3153 ± 0.0015 MHz
	B_6	−0.0004 ± 0.0001 MHz
	Dev.	12.4558 G/0.6250%
1GCF	g	1.9889 ± 0.0007
	B_4	−2.3023 ± 0.0080 MHz
	B_6	0.0010 ± 0.0019 MHz
	Dev.	9.5084 G/0.4749%

There are six stable isotopes of Gd, among which the isotopes with nuclear spin $I = 3/2$ have an abundance of 14.8% for ^{155}Gd and 15.65% for ^{157}Gd, and the rest of ^{154}Gd, ^{156}Gd, ^{158}Gd and ^{160}Gd have nuclear spin $I = 0$. However, hyperfine splitting induced by ^{155}Gd and ^{157}Gd is not observed in Fig. 1(a). The reason is that the hyperfine constants $A_{155} = 4.0$ G and $A_{157} = 5.34$ G,[46] both of which are smaller than the peak-to-peak width of 7 G of the spectral lines, and thus the hyperfine structure is hidden in the spectral lines and not observed.

It is noteworthy that when trivalent cations are doped into CaF_2 crystals, F^- ions are introduced into the interstitial positions to satisfy the charge balance of the system.[47] Due to the different positions of the interstitial F^- ions, the doping positions of the rare earth ions become unequal, where the most typical way of charge compensation is to introduce an interstitial F^- in the nearest neighbor position (NN) of the trivalent cation to form a locally symmetric structure of C_{4v}. In our samples, only Gd^{3+} with a local symmetry of O_h was observed. Friedman and Low found, by varying the annealing process, that these differences were mainly related to the rate at which the temperature of the crystals decreased during the thermal gradient and/or annealing process.[48] In fast-growing (0.5 to 1 inch per hour) crystals, the excess F^- does not have sufficient time to diffuse to more energetically stable sites near the trivalent ions, and Gd^{3+} tends to show cubic symmetry.

4.2 Effect of Gd doping concentration on local structure

At higher doping concentrations, exchange interaction (EI) occurs between Gd^{3+}–Gd^{3+}, which is caused by orbital overlap, and if the magnetic orbital orientation between the two ions favors the formation of the largest possible overlap integrals, then the exchange coupling constant $J < 0$, results in the formation of an antiferromagnetic coupling, and the ground state $|S_1–S_2| = 0$, and the number of unpaired electrons in the system $S_{eff} = 0$, *i.e.*, the EPR silent state. The reason that the

integral area of the EPR spectral line of 5GCF in Fig. 2(b) is smaller than that of 1GCF is that the exchange interaction between Gd^{3+}–Gd^{3+} leads to the EPR signal quench of most of the Gd^{3+} in 5GCF. The exchange interaction causes the EPR peak-to-peak width broadening. At the same time, there is a magnetic dipole–dipole interaction (MDDI) between Gd^{3+}. In high concentration samples, MDDI also leads to the broadening of the EPR spectrum. The higher the spin concentration, the shorter the inter-spin distance, the stronger the MDDI, the more efficient the energy relay transfer, and the larger the spectrum broadening.[49] Therefore, in Fig. 2(b), it is observed that the EPR spectra gradually broaden with increasing concentration (ESI Fig. 2†). Comparison of the concentration and the integral area of the EPR lines of the samples with different concentrations shows that the concentration of the NCF, 0.1GCF and 1GCF samples is proportional to the integral area (ESI Fig. 3†) suggesting that the other EPR lines in the 0.1GCF belong to other impurity ions. Among them, 7 spectral lines at 2316 G, 2768 G, 2906 G, 3550 G, 4162 G, 4342 G and 4776 G may be cubic Eu(II) signals (ESI Fig. 6†),[50] and the remaining impurity signals need to be further studied. For the GCF crystals grown from the same batch, similar EPR resonance lines for impurities were observed in 0.1GCF and 1GCF, and the EPR resonance lines for 5GCF were severely broadened, so no impurity peaks were observed, and thus the impurities were presumed to be from the feedstock.

For the shift of the EPR spectral line with the concentration of Gd ions in the sample observed in Fig. 2(b), we have fitted it using the open-source MATLAB program package *easyspin*,[51] and the results are shown in Table 3. It can be seen that the absolute value of the fourth-order crystal field parameter B_4 gradually decreases with increasing doping concentration. According to the experimental results of XRD in Fig. 2(c), the lattice constants given are also listed in Table 3. From the results in Table 3, it can be seen that the lattice constants increase gradually as the doping concentration is elevated, the distance between the Gd^{3+} and the surrounding F^- ions is gradually increased, and the effect of the crystal field on the Gd^{3+} is weakened, which leads to a gradual decrease in the crystal field splitting of the EPR lines.

The EPR lines in the center of NCF, 0.1GCF, 1GCF and 5GCF were fitted, and it was found that the EPR lines of NCF, 1GCF and 5GCF were Lorentzian line shape, while the spectral lines of 0.1GCF were Gaussian line shape (ESI Fig. 4†). When the spin concentration is very low, the EPR transition depends only on the spin-lattice interaction, and the absorption peak is Lorentzian line shape, which accords with our judgment that Gd^{3+} in NCF are all monomers. With the increase of doping concentration, spin–spin interaction results in Gaussian line shape of 0.1GCF. The doping concentration increases further, exchange interaction between neighbors exceeds the purely dipole interaction, the effects produced by exchange interaction are complex. If the spins are identical, the line is narrowed in the center and extended in the wings. This phenomenon is called 'exchange narrowing', and the shape approximates to a Lorentzian line shape.[44]

Table 3 Doping concentration, fourth-order and sixth-order zero-field splitting parameters and lattice constant of 5GCF, 1GCF and 0.1GCF obtained by *easyspin*

	Gd (at%)	B_4 (MHz)	B_6 (MHz)	Lattice constant (Å)
5GCF	5.75	−2.24163	−0.00059	5.4828
1GCF	1.22	−2.29283	−0.00017	5.4664
0.1GCF	0.17	−2.29983	−0.00050	5.4631
CaF_2				5.4619

The excitation and PL spectra of the samples are shown in Fig. 2(c) and (d). The energy state with orbital angular momentum $L = 1$ and spin $S = 5/2$ is split into $^6P_{3/2}$, $^6P_{5/2}$ and $^6P_{7/2}$ state, the energy state with orbital angular momentum $L = 2$ and spin $S = 5/2$ is split into $^6D_{5/2}$, $^6D_{7/2}$ and $^6D_{9/2}$ state, and the energy state with orbital angular momentum $L = 6$ and spin $S = 5/2$ is split into $^6I_{7/2}$, $^6I_{11/2}$, $^6I_{13/2}$, $^6I_{15/2}$ and $^6I_{17/2}$ state by the spin–orbit interaction. In the excitation spectra, $^6I_{11/2}$, $^6I_{13/2}$ and $^6I_{15/2}$ are combined in the absorption peak of 273.0 nm because of their similar energies. In the PL spectra, the emission bands $^6P_{5/2} \rightarrow {}^8S_{7/2}$ and $^6P_{7/2} \rightarrow {}^8S_{7/2}$ can be observed. Under the action of the crystal field, the transition at $^6P_{7/2} \rightarrow {}^8S_{7/2}$ appears to have several peaks.[52] At 16 K, three absorption peaks at 310.7 nm, 311.6 nm and 312.1 nm were observed, which correspond to the emission peaks of cubic configuration Gd^{3+} as reported.[53] The fine structure of the Gd^{3+} PL spectrum changes with increasing doping concentration, and the strongest emission peak gradually changes from 314.2 nm to 310.7 nm, which further demonstrates the change of the local crystal field structure of Gd^{3+}.[53]

With the increase of doping concentration, the widening, quenching and line shape changes of the EPR lines show a strong EI and MDDI between Gd^{3+}, and the changes in the fine structure of the excitation and PL spectra show the changes in the local crystal field structure of Gd^{3+}. Theoretical findings suggest that monomers tend to aggregate to form high-order clusters to make the fluorite system more stable,[54–56] which, in combination with the above experimental results, explains the formation of Gd^{3+} clusters.

4.3 Theoretical calculations of Gd^{3+}–Gd^{3+} dimer

The distribution and configuration of Gd^{3+}–Gd^{3+} in Gd^{3+} clusters are further analyzed using theoretical calculations.[57] For simplicity, two Gd^{3+} are considered to occupy the Ca^{2+} center lattice position separately, and the point group symmetries are both cubic, *i.e.*, the magnetic equivalence case. For the Gd^{3+}–Gd^{3+} ion pair occupying the cubic symmetric magnetic equivalence, its spin Hamiltonian under the external magnetic field B can be written as:

$$H_{\text{pair}} = S^{\text{A}} \cdot g_{\text{eff}} \cdot B + S^{\text{B}} \cdot g_{\text{eff}} \cdot B - 2J(R) \cdot S^{\text{A}} \cdot S^{\text{B}} + S^{\text{A}} \cdot K \cdot S^{\text{B}} \quad (2)$$

S^{A} and S^{B} are the equivalent spins of the two Gd^{3+} ions, and $J(R)$ is the isotropic exchange interaction coefficient, which is generally related to the distance R between the ions and decreases with increasing R. Anisotropic exchange interactions

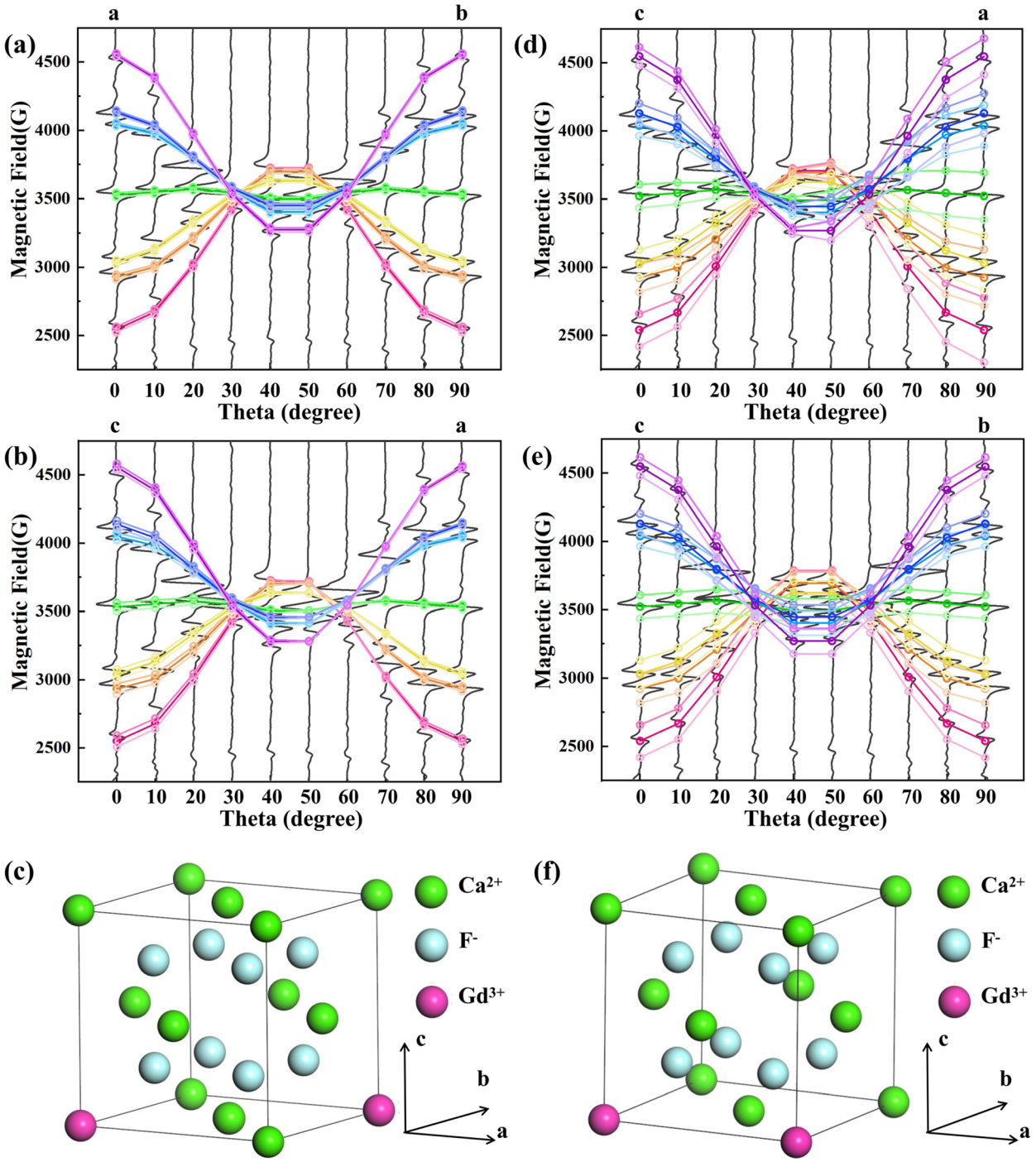

Fig. 3 Theoretical calculations of EPR spectral lines with magnetic field angle in the (a) *ab* plane and (b) *ac* plane for Gd^{3+}–Gd^{3+} distance $R = 7.7$ Å; (c) Gd^{3+}–Gd^{3+} ion pair orientation parallel to the [110]; theoretical calculations of EPR spectral lines with magnetic field angle in the (d) *ac* plane and (e) *bc* plane for Gd^{3+}–Gd^{3+} distance $R = 5.44$ Å; (f) Gd^{3+}–Gd^{3+} ion pair orientation parallel to the [100] direction.

are neglected here. K is the matrix of magnetic dipole–dipole interaction coefficients.

The essence of the above spin Hamiltonian quantity (2) is first to project the two energy levels corresponding to each EPR spectral line of an isolated Gd^{3+} ion into a subspace with an equivalent spin S of 1/2 (g_{eff} is its equivalent g-factor), and then it is equivalent to consider the effect of the exchange interaction J and the magnetic dipole interaction K on the spectral lines between two ion pairs with equivalent spins of 1/2. Using the energy ΔE between the corresponding two energy levels in combination with the EPR spectral resonance condition: $\Delta E(B) = h\nu$, the location of the magnetic field of the EPR spectral resonance of the corresponding Gd^{3+}–Gd^{3+} ion pair can be determined by the analytic formulas given in ref. 54.

Based on the crystal structure of CaF_2, two dimer cases are considered, (1) Gd^{3+}–Gd^{3+} ion pair with distance $R = 7.7$ Å and ion pair spatial orientation along the [110] direction, as in Fig. 3(c); (2) Gd^{3+}–Gd^{3+} ion pair with distance $R = 5.44$ Å and ion pair spatial orientation along the [100] direction, as in Fig. 3(f). Taking the position of the monomer Gd^{3+} EPR lines in the NCF as the position before splitting and considering only the interactions, it is calculated that the seven EPR lines of the Gd^{3+} ion split in response to EI and MDDI between the ion pairs. As shown in Fig. 3(a), (b), (d) and (e), the dark gray solid lines are the experimentally measured EPR lines, and the colored hollow circles are the theoretically calculated EPR line positions, where the three hollow circles of the same angle and the same color scheme indicate the EPR line positions of the Gd^{3+} monomer as well as the theoretically calculated positions of the two EPR lines of the split, respectively. The isotropic exchange interaction does not change the positions of the spectral lines. Two split resonance lines are not observed due to the widening of the EPR lines. Because the effect of the crystal field on the Gd^{3+} between NCF and 1GCF is different, there is a deviation between the theoretically calculated EPR lines positions and the measured EPR lines positions of 1GCF. Calculations show that the EPR line splitting values are comparable to the peak-to-peak width of the EPR lines of 1GCF when the Gd^{3+}–Gd^{3+} ion pair distance $R = 7.7$ Å and along the [110] direction, as shown in Fig. 3(a) and (b). When the Gd^{3+}–Gd^{3+} ion-pair distance $R = 5.44$ Å and along the [100] direction, the EPR line splitting value differs from the peak-to-peak width of the EPR line of 1GCF, as shown in Fig. 3(d) and (e). Only a single Lorentzian peak was obtained by fitting the center peak shape of 1GCF, suggesting that the majority of Gd^{3+} in 1GCF is distributed as a dimer conformation along the [110] direction and at a distance about 7.7 Å.

After Gd^{3+} substitution for Ca^{2+}, the structural relaxation is small, the symmetry is hardly broken, and the cubic conformation remains (Fig. 4), which is in accordance with the EPR fitting results of 1GCF. The bond length between Ca^{2+} and F^- in the normal lattice is 2.365 Å. After a single Gd^{3+} replaces Ca^{2+}, the bond length between Gd^{3+} and F^- becomes 2.328 Å, which is slightly reduced compared with the intact crystal. After the substitution of two Gd^{3+} for Ca^{2+}, the bond length of Gd^{3+} with F^- becomes 2.373 Å, which is slightly increased. The reason is that the Bader charge of Gd^{3+} after a single Gd^{3+} replaces Ca^{2+} (6.828*e*) is smaller than that of Gd^{3+} after two Gd^{3+} replaces Ca^{2+} (7.060*e*), *i.e.*, the former carries a higher positive charge, and there is a larger coulombic gravitational force between Gd^{3+} and F^-, and therefore, the former has a shorter bond length. The shorter bond length of Gd^{3+} with F^- in dimer suggests that there is less crystal-field interaction in 1GCF. The absolute value of the crystal field action parameter B_4 is smaller, consistent with the results of the EPR fits for NCF and 1GCF.

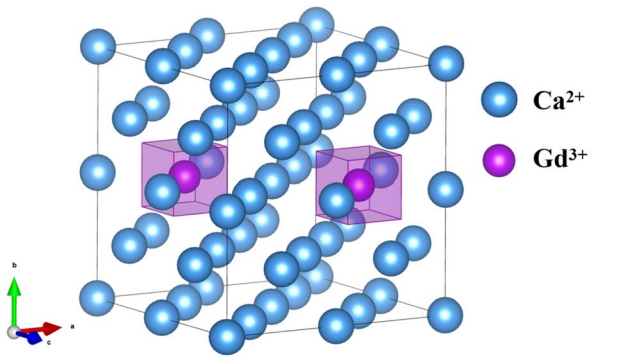

Fig. 4 A schematic diagram of a 2 × 2 × 2 supercell of the CaF_2 crystal (for clarity, F^- ions are removed from the figure), Gd^{3+}–Gd^{3+} ion pair orientation parallel to the [110].

5. Conclusions

In summary, we prepared four Gd:CaF_2 crystals in this work. The spin Hamiltonian of the 1.5 ppm Gd impurity sample shows that Gd^{3+} is in cubic conformation in CaF_2, which may be attributed to the fact that the F^-, which acts as a charge compensator, is located farther away from the center of Gd^{3+}. The results of EPR tests in the axial direction of Gd:CaF_2 crystals with different concentrations show that the signal intensity of the cubic conformation of Gd is enhanced and then weakened with increasing doping concentration, and the EPR lines are broadened, which indicates that the EI and MDDI between Gd^{3+}–Gd^{3+} are enhanced, and the distance between Gd^{3+}–Gd^{3+} is gradually shortened with the increase of doping concentration. The excitation and PL spectra show that the fine structure of the spectra changes with increasing doping concentration, which further proves that the crystal field of Gd^{3+} changes. Combining the test results of EPR and optical spectra, it can be hypothesized that Gd^{3+} aggregates to form cluster structures with increasing doping concentration. By fitting experimentally measured angular dependence data for 1.22 at% Gd:CaF_2 crystals, combined with theoretical calculations, it was obtained that most of the Gd^{3+} is in the dimer configuration distributed along the [110] direction and at a distance of 7.7 Å, and the Gd^{3+} remains cubic. The present work explains the variation of the localized structure of Gd^{3+} in CaF_2 matrix with concentration, which is of some reference value for the evolution of cluster structure of other rare earth ions in alkaline earth metal fluoride.

Data availability

The data supporting this study's findings are available from the corresponding author upon reasonable request.

Author contributions

Conceptualization, project administration and resources: Wei Hong and Liangbi Su. Data curation: Fang Tan. Formal analysis and software: Shirui Luo, Fang Tan and Liening Wei. Funding acquisition: Wei Hong, Liangbi Su, Huamin Kou and Dapeng Jiang. Investigation and validation: Shirui Luo performed the electron paramagnetic resonance test. Yu Liu performed the optical experiment. Huaize Qin, Jingguo Zhu and Junjie Hu prepared the crystal sample. Methodology: Honggang Liu

performed theoretical calculations of Gd^{3+}–Gd^{3+} pairs, and Tingyu Liu performed the DFT calculations. Supervision: Zhen Zhang, Fengkai Ma and Zhonghan Zhang. Visualization: Shrui Luo. Writing – original draft: Shirui Luo. Writing – review & editing: Wei Hong.

Conflicts of interest

There are no conflicts to declare.

Acknowledgements

This work has been financially supported by the National Key Technologies R&D Program (2022YFB3605701), the National Natural Science Foundation of China (U2230103, 61925508) and CAS Project for Young Scientists in Basic Research (YSBR-024).

References

1 H. Schwoerer, B. Liesfeld, H. P. Schlenvoigt, K. U. Amthor and R. Sauerbrey, *Phys. Rev. Lett.*, 2006, **96**, 014802.
2 U. Keller, *Nature*, 2003, **424**, 831–838.
3 R. A. Snavely, M. H. Key, S. P. Hatchett, T. E. Cowan, M. Roth, T. W. Phillips, M. A. Stoyer, E. A. Henry, T. C. Sangster, M. S. Singh, S. C. Wilks, A. MacKinnon, A. Offenberger, D. M. Pennington, K. Yasuike, A. B. Langdon, B. F. Lasinski, J. Johnson, M. D. Perry and E. M. Campbell, *Phys. Rev. Lett.*, 2000, **85**, 2945–2948.
4 E. L. Clark, K. Krushelnick, M. Zepf, F. N. Beg, M. Tatarakis, A. Machacek, M. I. K. Santala, I. Watts, P. A. Norreys and A. E. Dangor, *Phys. Rev. Lett.*, 2000, **85**, 1654–1657.
5 D. Strickland and G. Mourou, *Opt. Commun.*, 1985, **55**, 447–449.
6 A. A. Kuzmin, E. A. Khazanov, O. V. Kulagin and A. A. Shaykin, *Opt. Express*, 2014, **22**, 20842–20855.
7 K. Ertel, C. Hooker, S. J. Hawkes, B. T. Parry and J. L. Collier, *Opt. Express*, 2008, **16**, 8039–8049.
8 R. Soulard, D. Stoffel, J.-L. Doualan, A. Braud, S. Montant, J.-P. Goossens, P. Camy, in *Laser Congress 2018 (ASSL)*, Optica Publishing Group, Boston, Massachusetts, 2018, p. ATu2A.18.
9 J. Zhu, L. Wei, W. Tian, J. Liu, Z. Wang, L. Su, J. Xu and Z. Wei, *Laser Phys. Lett.*, 2016, **13**, 055804.
10 S. Wang, D. Jiang, Q. Wu, S. Pang, J. Wang, X. Qian, J. Liu, B. Mei and L. Su, *J. Alloys Compd.*, 2019, **781**, 629–632.
11 F. K. Ma, D. P. Jiang, L. B. Su, J. Y. Wang, W. Cai, J. Liu, J. G. Zheng, W. G. Zheng, J. Xu and Y. Liu, *Opt. Lett.*, 2016, **41**, 501–503.
12 A. A. Kaminskii, V. V. Osico, A. M. Prochorov and Y. K. Voronko, *Phys. Lett.*, 1966, **22**, 419–421.
13 A. Kaminskii, *Zhetf Pisma Redaktsiiu*, 1967, **6**, 615.
14 A. A. Kaminskii, N. R. Agamalyan, G. A. Deniseneo, S. E. Sarkisov and P. P. Fedorov, *Phys. Status Solidi A*, 1982, **70**, 397–406.
15 K. S. Bagdasarov, Y. K. Voronko, A. A. Kaminskii, L. V. Krotova and V. V. Osiko, *Phys. Status Solidi B*, 1965, **12**, 905–912.
16 Z. P. Qin, G. Q. Xie, J. Ma, W. Y. Ge, P. Yuan, L. J. Qian, L. B. Su, D. P. Jiang, F. K. Ma, Q. Zhang, Y. X. Cao and J. Xu, *Opt. Lett.*, 2014, **39**, 1737–1739.
17 X. Tang, J. Qiu, Z. Fan, L. Su and H. Wang, *Opt. Mater.*, 2016, **58**, 445–448.
18 M. Abraham, R. A. Weeks, G. W. Clark and C. B. Finch, *Phys. Rev.*, 1965, **137**, A138–A142.
19 J. Stäblein, K. Pöhl, A. Weisleder, G. v. d. Gönna, T. Töpfer, J. Hein and M. Siebold, Optical Properties of CaF_2 and Yb^{3+}:CaF_2 for Laser Applications, *Proc. SPIE*, 2011, **8080**, 808002.
20 S. Zhang, L. Wang, G. Zhu, M. Diehl, A. Maldar, X. Shang and X. Zeng, *Int. J. Plast.*, 2022, **150**, 103186.
21 C. R. A. Catlow, A. V. Chadwick, G. N. Greaves and L. M. Moroney, *Nature*, 1984, **312**, 601–604.
22 Y. K. Voron'ko, A. A. KAminskii and V. V. Osiko, *JETP Lett.*, 1965, **2**, 294.
23 D. R. Tallant and J. C. Wright, *J. Chem. Phys.*, 1975, **63**, 2074–2085.
24 C. Andeen, D. Link and J. Fontanella, *Phys. Rev. B*, 1977, **16**, 3762–3767.
25 C. R. A. Catlow, A. V. Chadwick and J. Corish, *J. Solid State Chem.*, 1983, **48**, 65–76.
26 A. K. Cheetham, B. E. F. Fender and M. J. Cooper, *J. Phys. C: Solid State Phys.*, 1971, **4**, 3107–3121.
27 F. Ma, F. Su, R. Zhou, Y. Ou, L. Xie, C. Liu, D. Jiang, Z. Zhang, Q. Wu, L. Su and H. Liang, *Mater. Res. Bull.*, 2020, **125**, 110788.
28 F. Ma, Z. Zhang, D. Jiang, Z. Zhang, H. Kou, A. Strzep, Q. Tang, H. Zhou, M. Zhang, P. Zhang, S. Zhu, H. Yin, Q. Lv, Z. Li, Z. Chen and L. Su, *Cryst. Growth Des.*, 2022, **22**, 4480–4493.
29 F. Ma, H. Zhou, Q. Tang, L. Su, M. Zhang, P. Zhang, H. Yin, Z. Li, Q. Lv and Z. Chen, *J. Alloys Compd.*, 2022, **899**, 162913.
30 G. Vincow and W. Low, *Phys. Rev.*, 1961, **122**, 1390–1392.
31 M. J. Weber and R. W. Bierig, *Phys. Rev.*, 1964, **134**, A1492–A1503.
32 U. Ranon and J. S. Hyde, *Phys. Rev.*, 1966, **141**, 259–274.
33 E. S. Sabisky, *Phys. Rev.*, 1966, **141**, 352–362.
34 F. M.-t. Lay and A. W. Nolle, *Phys. Rev.*, 1967, **163**, 266–275.
35 J. Kirton and S. D. McLaughlan, *Phys. Rev.*, 1967, **155**, 279–284.
36 M. R. Brown, K. G. Roots, J. M. Williams, W. A. Shand, C. Groter and H. F. Kay, *J. Chem. Phys.*, 1969, **50**, 891–899.
37 L. K. Aminov, I. N. Kurkin, A. V. Lovchev, R. M. Rakhmatullin, A. A. Rodionov and S. L. Korableva, *Mater. Chem. Phys.*, 2020, **240**, 122136.
38 S. A. Kazanskii, A. I. Ryskin, A. E. Nikiforov, A. Y. Zaharov, M. Y. Ougrumov and G. S. Shakurov, *Phys. Rev. B:Condens. Matter Mater. Phys.*, 2005, **72**, 014127.
39 S. M. Saini, N. Singh, T. Nautiyal and S. Auluck, *Solid State Commun.*, 2006, **140**, 125–129.
40 W. Low, *Phys. Rev.*, 1958, **109**, 265–271.
41 C. Ryter, *Helv. Phys. Acta*, 1957, **30**, 353–373.
42 S. Lee, A. J. Bevolo and C.-C. Yang, *J. Chem. Phys.*, 1974, **60**, 1628–1633.

43 J. M. Baker, B. Bleaney and W. Hayes, *Proc. R. Soc. London, Ser. A*, 1958, **247**, 141–151.
44 A. Abragam, B. Bleaney, *Electron Paramagnetic Resonance of Transition Ions*, 1970, pp. 52–60.
45 O. Vahtras, B. Minaev and H. Ågren, *Chem. Phys. Lett.*, 1997, **281**, 186–192.
46 W. Low, *Phys. Rev.*, 1956, **103**, 1309.
47 S. Fang, Q. Zhang, *Crystal Color Center Physics*, Shanghai, Shanghai Jiao Tong University Press, 1989.
48 E. Friedman and W. Low, *J. Chem. Phys.*, 1960, **33**, 1275–1276.
49 J. Su, J. Du, *Electron Paramagnetic Resonance Spectroscopy: Principles and Applications*, Beijing, Science Press, 2022.
50 R. S. Title, *Phys. Lett.*, 1963, **6**, 13–14.
51 S. Stoll and A. Schweiger, *J. Magn. Reson.*, 2006, **178**, 42–55.
52 H. M. Crosswhite, R. L. Schwiesow and W. T. Carnall, *J. Chem. Phys.*, 1969, **50**, 5032–5033.
53 J. Makovsky, *Phys. Lett.*, 1966, **19**, 647–649.
54 J. Corish, C. R. A. Catlow, P. W. M. Jacobs and S. H. Ong, *Phys. Rev. B:Condens. Matter Mater. Phys.*, 1982, **25**, 6425–6438.
55 P. J. Bendall, C. R. A. Catlow, J. Corish and P. W. M. Jacobs, *J. Solid State Chem.*, 1984, **51**, 159–169.
56 C. R. A. Catlow and M. J. Norgett, *J. Phys. C: Solid State Phys.*, 1973, **6**, 1325–1339.
57 H. Liu and W. Zheng, *J. Appl. Phys.*, 2018, **123**, 025105.